La mer 35: 35-47, 1997
Société franco-japonaise d'océanographie, Tokyo

Spatial distributions and mixing energies of tidal currents over the eastern Bering Sea shelf

Tomonori AZUMAYA* and Yutaka ISODA*

Abstract: The spatial semidiurnal and diurnal tides and their tidal currents over the eastern Bering Sea shelf were investigated by use of a two-dimensional barotropic model on f-plane. There is a different tidal response between the two main bays along the Alaska coast. The semidiurnal tidal current predominates in Bristol Bay, while the diurnal tidal current predominates in Norton Sound. The results of our model attribute this difference to that between the forcing periods of the respective co-oscillating tides. Furthermore, the model results suggest that the larger amplitudes of diurnal tidal current along the slope relative to those of the shelf area are caused by the topographic Rossby wave manner with energy trapping on the shelf slope. To spatially investigate the effect of the tidal energy on the mixing of water column, the potential energy anomaly was calculated using hydrographic data taken between 1963 and 1992. The tidal front forms along the coast of Alaska, where the potential energy anomaly is relatively small, and its location well corresponds to the spatial contour-lines of the critical parameter of log $(H/U^3)=2.5\sim3.0$ for the tidal mixing energy. It is inferred that the vertical mixing energy of tidal currents plays an important role in the formation of this coastal front there. However, the spatial configuration of the potential energy anomaly cannot be explained by the $\log(H/U^3)$ in the north of St. Lawrence Island, where the Anadyr Current flows across the shelf.

1. Introduction

The eastern Bering Sea shelf extends about 1,000 km from Unimak Pass in the southeast to Cape Navarin in the northwest. It is bounded by lands on three sides : the Alaskan Peninsula in the southeast, the Alaskan mainland in the northeast, and Siberia in the northwest (Fig. 1). With its surface area of 1.2×10^6 km^2, it is one of the widest ocean shelves known, and also boasts one of the world's most productive ocean ecosystems.

Current-meter records over the eastern Bering Sea shelf have shown that 60-95 % of the variance in the current's horizontal kinetic energy was the result of tidal components (SCHUMACHER and KINDER, 1983). The mean vector speeds of the shelf's current(<2 cm•s^{-1}) were one order of magnitude lower than the speeds of the tidal current (20 cm•s^{-1}). Hence, the shelf has become notorious for strong tidal currents.

Tidal waves enter the Bering Sea as free waves from the North Pacific Ocean, mainly through the central and western passages of the Aleutian-Komandorski Islands. The Arctic Ocean is a secondary source of tides which propagate southward into the north Bering Sea. PEARSON *et al.* (1991) used long-term direct current measurements to determine that the predominant semidiurnal tides, such as the M_2 and N_2 constituents, are seen throughout most of the shelf, while diurnal tides, such as the K_1 and O_1 constituents, predominate in the Norton Sound. Diurnal tides also predominate over the shelfbreak at the northeastern Bering Sea shelf (MOFJELD, 1986). Recently, SCHUMACHER and REED (1992) showed that the amplitudes of the K_1 tidal current (19.8 cm•s^{-1}) are larger than that of the M_2 tidal current (6.9 cm•s^{-1}) based on direct current measurements on the shelf slope.

A numerical model by SÜNDERMAN (1977) predicted the distribution of the M_2 constituent

* Faculty of Fisheries, Hokkaido University, 3-1-1 Minato-cho, Hakodate 041, Japan

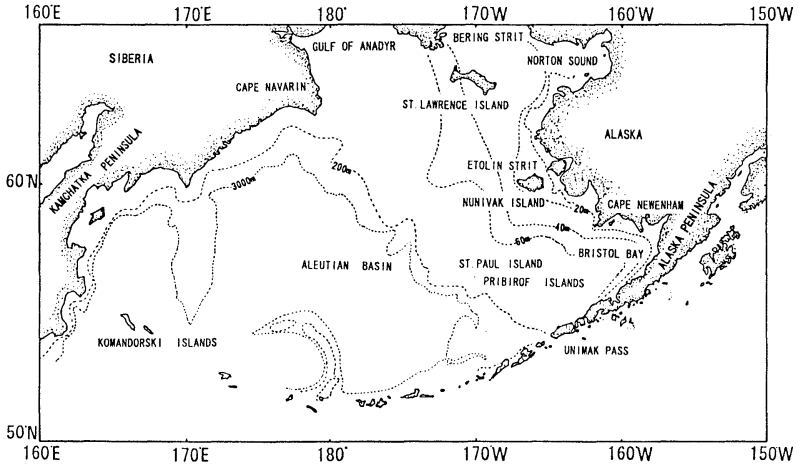

Fig. 1. Bottom topography of the Bering Sea.

in the Bering Sea, as well as the M_2 tidal current ellipses and tidal dissipation. The model resulted in a good quantitative agreement for the M_2 constituent. The three-dimensional model by LIU and LEENDERTSE (1982, 1986) also predicted the M_2 and K_1 constituents in the Bering and the Chuckchi Sea, though it did not predict either the diurnal tidal current of the whole shelf to add to the shelf slope or the spatial distributions of tidal mixing energy.

SCHUMACHER and KINDER (1979) investigated the structure of the tidal front along the coast of Alaska and its frontogenesis. This tidal front, the boundary between the mixed water of the coastal shallow region and the stratified water of the middle region, is about 20 km wide along the 50 m depth contour. Another tidal front, discovered in the vicinity of the British Isles, has been discussed by SIMPSON (1971, 1978), SIMPSON and HUNTER (1974), PINGREE *et al.* (1974), FEARNHEAD (1975) and JAMES (1977). These authors proposed that the tidal front might have been generated by an energy balance between tidally generated mixing and buoyancy input. SIMPSON and HUNTER (1974) suggested that the location of frontogenesis depends on a critical parameter $\log(H/U^3)$ for the mixing energy (H is the water depth in m and U the amplitude of tidal current in $m \cdot s^{-1}$). However, numerous aspects of the tidal current, including its spatial distributions and the relationship between the parameter $\log(H/U^3)$ and potential energy anomaly, have yet to be determined for most of the eastern Bering Sea shelf.

Accordingly, the purpose of the present study is to describe, using a numerical model, the characteristics of the distribution of the tide and tidal currents over the Bering Sea shelf and to examine how the distributions of $\log(H/U^3)$ correspond to the distributions of the potential energy anomaly over the shelf.

2. Mean field of temperature, salinity and density

Hydrographic data for the eastern Bering Sea shelf were obtained by T.S. Oshoromaru (Faculty of Fisheries, Hokkaido Univ., 1964 1993). The data were collected using Nansen bottles untill 1983, and by CTD since 1984. Figure 2 shows the number of hydrographic stations of inside $1° \times 1°$ quadrangles for 1963 ~1992 to describe the spatial mean distributions of temperature and salinity.

Figures 3(a), (b) and (c) show the averaged vertical section of temperature, salinity and density from 180° meridian to 159° W at along 59° N over the eastern Bering Sea shelf based on long-term successive observations over the summers of 1963~1992 (see Fig. 2 for its location). Thermocline lies at the depth of 20 m~ 30 m on the shelf edge. Cold water of less than 2℃ occupies the region from the shelfbreak to the middle shelf during the spring and summer (OHTANI, 1973 ; COACHMAN and CHARNELL, 1979). In the coastal shallow region of Alaska,

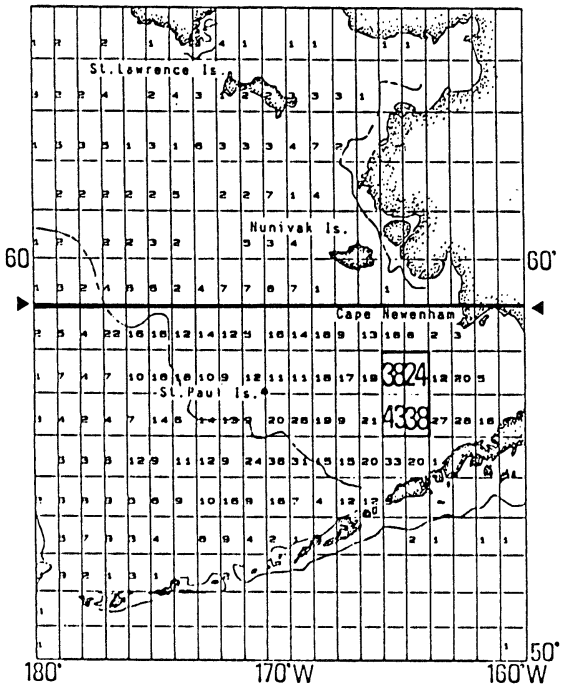

Fig. 2. Number of hydrocast and CTD in each quadrangle.

where the surface water temperature rises to 8℃, the water column is well-mixed and the water temperature near the bottom higher than 6℃. The water near the coast of Alaska has a salinity of less than 31 PSU and is fresher than offshore waters. The density structure almost depends on the salinity over the shelf region. Between the middle shelf and coastal region, there is a narrow transition separating the two-layered middle shelf region from the well-mixed coastal region. Therefore, the tidal front is a common feature in long term averaged vertical sections of water temperature, salinity and density.

3. Numerical simulations of tide

3.1 Model description

To obtain the spatial distributions of tides and tidal currents, we use the vertically integrated equation of motion and continuity in a Cartesian coordinate system :

$$\frac{\partial \boldsymbol{u}}{\partial t}+(\boldsymbol{u}\cdot\nabla)\boldsymbol{u}+f\boldsymbol{k}\times\boldsymbol{u} = -g\nabla\zeta-\frac{\gamma_b^2|\boldsymbol{u}|\boldsymbol{u}}{H+\zeta}+A_h\nabla^2\boldsymbol{u} \quad (1)$$

$$\frac{\partial \zeta}{\partial t}+\nabla\cdot\{(H+\zeta)\boldsymbol{u}\} = 0 \quad (2)$$

where $\boldsymbol{u}$ is the depth-averaged vecolity, t the time, ∇ the horizontal differential operator, $\boldsymbol{k}$ the vertical unit vector, g ($=980$ cm$\cdot$s^{-2}) the gravitational acceleration, ζ the sea surface elevation above the mean sea surface, γ_b^2 ($=0.0026$) the bottom frictional coefficient, A_h ($=10^7$ cm$^2\cdot$s^{-1}) the coefficient of horizontal eddy viscosity, H the water depth and the f the Coriolis parameter at 60° N ($f=1.25\times10^{-4}$ s^{-1}). Here, the validity of the f model for a simulation in this region may be checked by estimating planetary-beta $\beta_p=1\times10^{-13}$ cm$^{-1}\cdot$s^{-1} (the meridional gradient of f) and topographic-beta $\beta_t=5\times10^{-12}$ cm$^{-1}\cdot$s^{-1} ($=\frac{f}{H}\cdot\frac{dH}{dx}$). Thus, the topographic β_t is dominant by at least one order, and β_p may be ignored relative to β_t.

This model sea is covered by a quadratical grid of 50 km×50 km. As shown in Fig. 4, the model incorporates the actual bathymetry of the eastern Bering Sea region, taking its bathymetric data from a chart published by

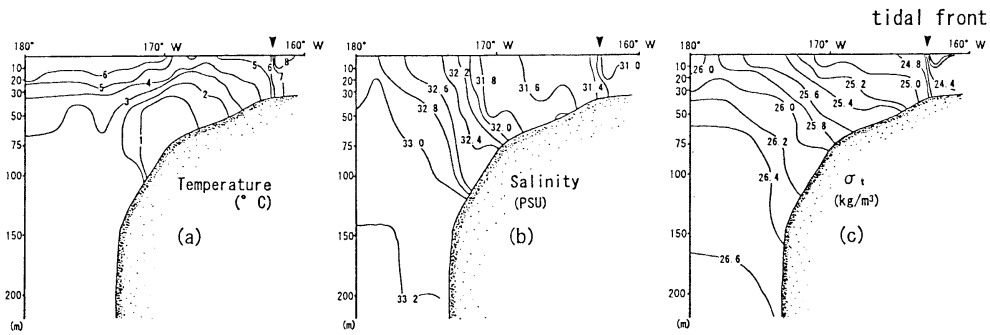

Fig. 3. Mean vertical distributions of temperature (a), salinity (b) and density (c) at latitude of 59° N (line in Fig. 2).

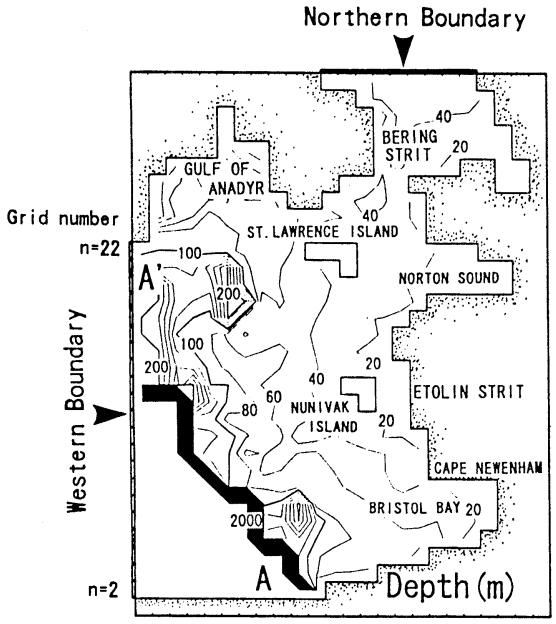

Fig. 4. Bottom topography of the eastern Bering Sea shelf (contours are in m). The model basin with a depth of more than 2000 m is assumed to be 2000 m constant.

the Japan Maritime Safety Agency. This results in two distinct domains : a deep basin and relatively shallow shelf.

The M_2 and K_1 constituents are dominant over the eastern Bering Sea shelf. These two tidal constituents are the only ones included in the computations, both because their amplitudes are larger than those of N_2 and O_1, respectively, and because their cotidal and corange charts are very similar to those for N_2 and O_1 tides (PEARSON *et al.*, 1981). Here, the M_2 and K_1 constituents are generally representative of the semidiurnal and diurnal tides. The observed tidal amplitude and phase lag (Fig. 4) are given along two open boundaries to the west of the eastern Bering Sea shelf and the Bering Strait as located using cotidal charts by SÜNDERMAN (1977) and PEARSON *et al.* (1981). Table 1 shows the harmonic constants in two open boundaries. The tidal elevations across the two open boundaries are specified as cosines :

$$\zeta = A \cdot \cos(\omega t - G) \qquad (3)$$

where A is the amiplitudes, G the Greenwich phase lags, and ω the angular frequency. The

Table 1 Harmonic constants in boundaries.

	M_2		K_1	
	a (cm)	G	a (cm)	G
West boundary	20	70–0.8n	30	330
North boundary	7	231	20	310

a : amplitude (cm) G : phase (degree)
n : grid number

harmonic constants of the tidal currents are determined by harmonic analyses of the current records of SÜNDERMAN (1977), PEARSON *et al.* (1981), MOFJELD (1986), and SCHUMACHER and REED (1992). Equations (1) and (2) were approximated by the finite-differences and solved by the primitive method. The tidal model ran for a simulation time of 10 days until the solution showed no significant changes from cycle to cycle. The sea surface elevation and velocity were sampled every hour. These data were then used to perform the harmonic analysis to determine the tidal constants and current ellipse parameters.

3.2 Model results

Semidiurnal and diurnal tides

Spatial distributions of observed cotide and corange lines for the M_2 constituent are shown in Fig. 5(a). The three amphidromic points of the M_2 tide located near Cape Newenham, in Norton Sound, and southeast of St. Lawrence Island. The amplitudes of M_2 tide varied from 40 cm off the mouth of Bristol Bay to 120 cm along the coast of the Alaskan mainland. On the other hand, in Norton Sound the amplitudes were less than 10 cm, smaller than those in Bristol Bay. Figure 5(b) shows the spatial distributions of the calculated cotide and corange lines for the M_2 constituent. The calculated amphidromic points locate at the same positions as the observed ones. In addition to these three points, the model predicts the existence of an amphidromic point off the Gulf of Anadyr and one in the Bering Strait. The calculated amplitude in Bristol Bay is 120 cm, larger than that in Norton Sound. The calculated phase lines in the Etolin Strait change abruptly

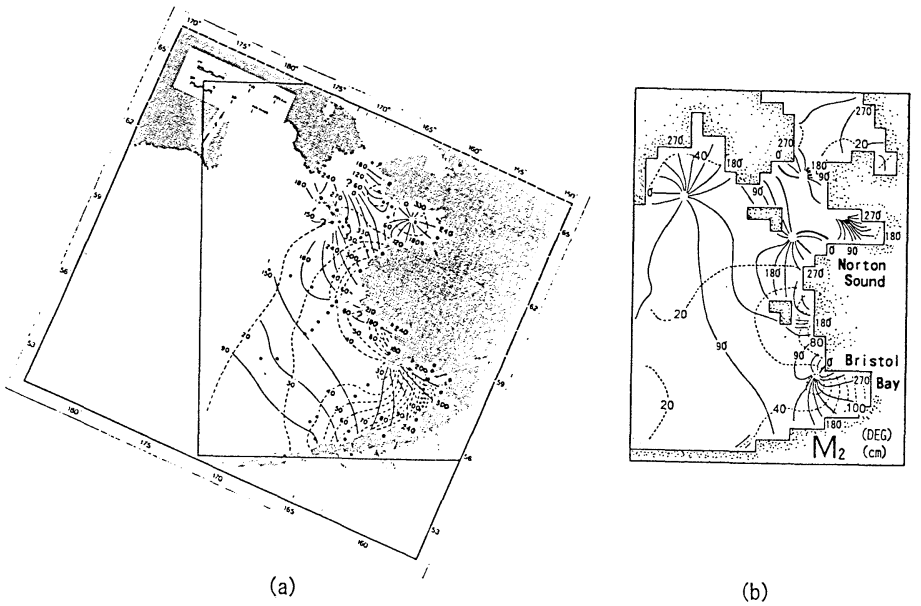

Fig. 5. (a) Observed cotidal map for M_2 tide (PEARSON *et al.*, 1981). (b) Model-predicted cotidal map for the M_2 tide. Solid lines are cotide lines referenced to Greenwich in degrees. Broken lines are corange lines in cm.

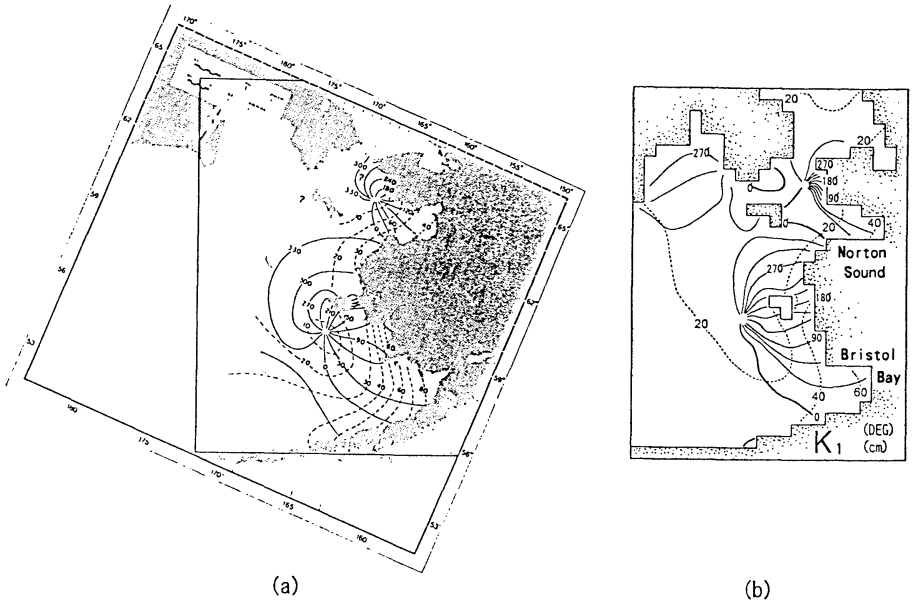

Fig. 6. (a) Same as Fig. 5(a) but for K_1. (b) Same as Fig. 5(b) but for K_1.

between the north and south ends.

Spatial distributions of the observed cotide and corange lines for the K_1 constituent are shown in Fig. 6(a). One of the two amphidromic points of the K_1 tide located west of Norton Sound, and other point in the area between Nunivak Island and the Pribilof Islands. The maximum amplitude of the K_1 tide in Bristol Bay was about 60 cm, and in Norton Sound was about 40 cm. Figure 6(b) shows the

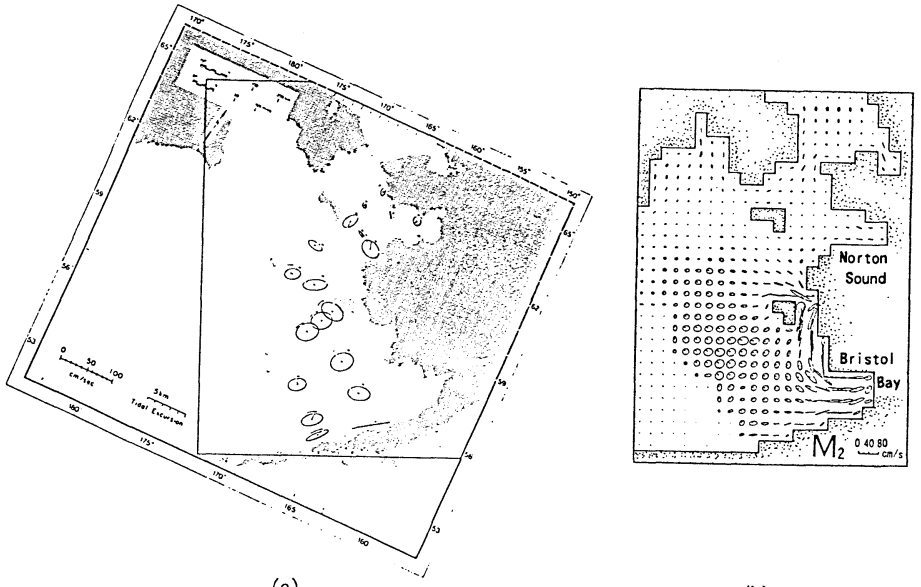

Fig. 7. (a) Observed tidal current ellipses for M_2 (PEARSON *et al.*, 1981). (b) Model-predicted tidal current ellipses for M_2.

spatial distributions of the calculated cotide and corange lines for the K_1 tide. The amphidromic points locate at the same area in the observed cotide lines. The phase and amplitude distributions of the calculated diurnal tide are highly similar to the observed ones.

Semidiurnal and diurnal tidal currents

Figure 7(a) shows the spatial distributions of observed tidal current ellipses for the M_2 constituent. The observed M_2 tidal current ellipses over the shelf were almost circular, and exhibited a clockwise rotation. However, there were two exceptions, one near the Alaskan Peninsula, where the ellipses had a nearly rectilinear motion, and the other in Bristol Bay, where the rotation was anticlockwise. Figure 7(b) shows the distributions of calculated tidal current ellipses for the M_2 constituent. They are almost identical to those of the observed ones. The rotation of the observed tidal current ellipses is well reproduced by the numerical model. At the mouth of Bristol Bay, the major axes of these predicted ellipses have a maximum speed of 30~40 cm•s^{-1}, while in Norton Sound the maximum speed of tidal current is less than 20 cm•s^{-1}. The model predicts tidal-current amplitudes of more than 40 cm•s^{-1} in the Etolin Strait, where the predicted amplitudes is largest in the whole region.

Figure 8(a) shows the observed tidal current ellipses for the K_1 constituent. They rotate nearly clockwise and are elongated to form a straight line, unlike the nearly circular tidal ellipses of M_2. The observed amplitudes of K_1 over the shelf are 10~15 cm•s^{-1} and almost smaller than the tidal ellipses of M_2 with the exception of those in Norton Sound. The amplitudes of the K_1 tidal current in Bristol Bay are as large as those over the shelf. On the other hand, the amplitudes of the tidal current in Norton Sound are larger than 30 cm•s^{-1}. The calculated K_1 tidal-current ellipses distribute like the observed ones, as shown in Fig. 8(b). Our model also reproduces these differences of predominant tidal current in each bay. The ellipses along the shelf slope become circular and their maximum amplitudes are over 40 cm•s^{-1}, although the calculated phase and amplitudes of K_1 tidal currents vary widly.

4. Discussions

4.1 Tidal currents in Bristol Bay and Norton Sound

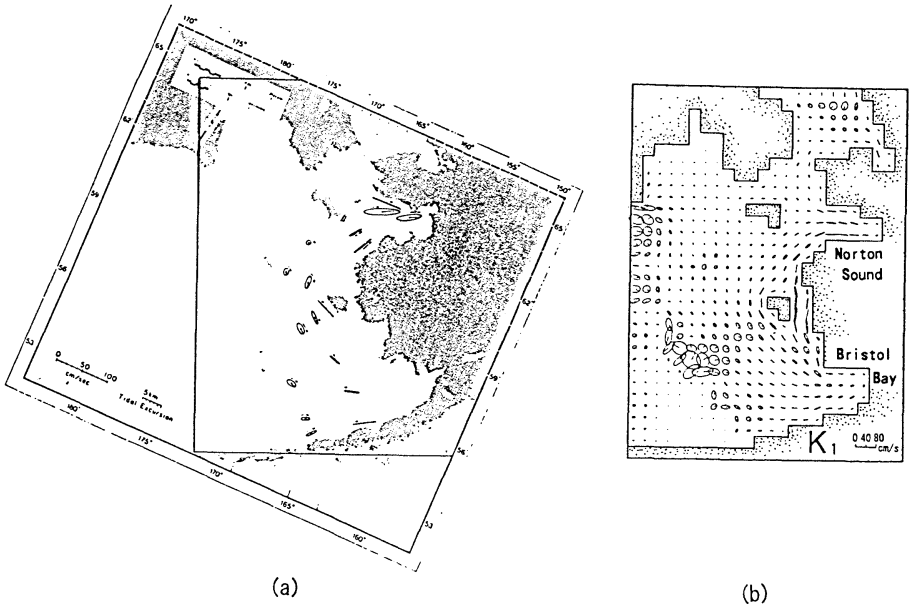

Fig. 8. (a) Same as Fig. 7(a) but for K_1. (b) Same as Fig. 7(b) but for K_1.

PEARSON *et al.* (1981) proposed that the small semidiurnal tidal current in Norton Sound might have been the result of bottom friction across the broad Bering Sea shelf, and that the diurnal tidal current in Norton Sound was larger than that in Bristol Bay because of the shallower depth. However, if bottom friction dissipated tidal current, then the amplitude of not only the semidiurnal tidal current but also the diurnal tidal current must be small in Norton Sound than in Bristol Bay. Since PEARSON *et al.* (1981) also reported that the diurnal tide /tidal current phase relationship indicated predominantly standing wave characteristics in Norton Sound, we suspected that the co-oscillating tide was associated with the position of amphidromic points in both Bristol Bay and Norton Sound. To examine the cause of the different behaviors of tidal current in both locations, we used the simple one-dimensional co-oscillating tidal models shown in Figs. 9(a) and (b). The length l of both Bristol Bay and Norton Sound is 250 km(the mouth of the bay is $x=0$), where x is the coordinate defined along the longitudinal axis of the bay. The depth h of Norton Sound is 20 m. On the other hand, in the case of Bristol Bay, with its constant bottom slope and a water depth determined as $h=2h_m(1-x/l)$, the mean water depth is $h_m=40$ m. The tide is assumed to oscillate by the elevation a_m at the mouth of the bay for each forcing period. Here, a_m is the observed amplitude of the tide, and the given a_m at the mouth of Bristol Bay and Norton Sound are 40 cm and 10 cm, respectively. These a_m are constant for each forcing period. The case for Norton Sound is given by Eqs. (4) and (5), below.

$$\eta(x) = a_m \cdot \frac{\cos(k(l-x))}{\cos(kl)} \tag{4}$$

$$u(x) = a_m \cdot \frac{C}{h} \cdot \frac{\sin(k(l-x))}{\cos(kl)} \tag{5}$$

The standing oscillation in the linear case for Bristol Bay is given by Eqs.(6) and (7)(UNOKI and ISOZAKI, 1965) :

$$\eta(x) = a_m \cdot \frac{J_0(\sqrt{2}\,kl\sqrt{1-x/l})}{J_0(\sqrt{2}\,kl)} \tag{6}$$

$$u(x) = \frac{a_m \cdot C}{\sqrt{2}\,h_m\sqrt{1-x/l}} \cdot \frac{J_1(\sqrt{2}\,kl\sqrt{1-x/l})}{J_0(\sqrt{2}\,kl)} \tag{7}$$

where J_0 and J_1 the zero- and the first-order Bessel functions, $\eta(x)$ the elevation, $u(x)$ the velocity, g the gravitational acceleration, C the propagation speed of phase for gravity wave ($\sqrt{gh}$), k the wave number($2\pi/C\times T$), and T the forcing period.

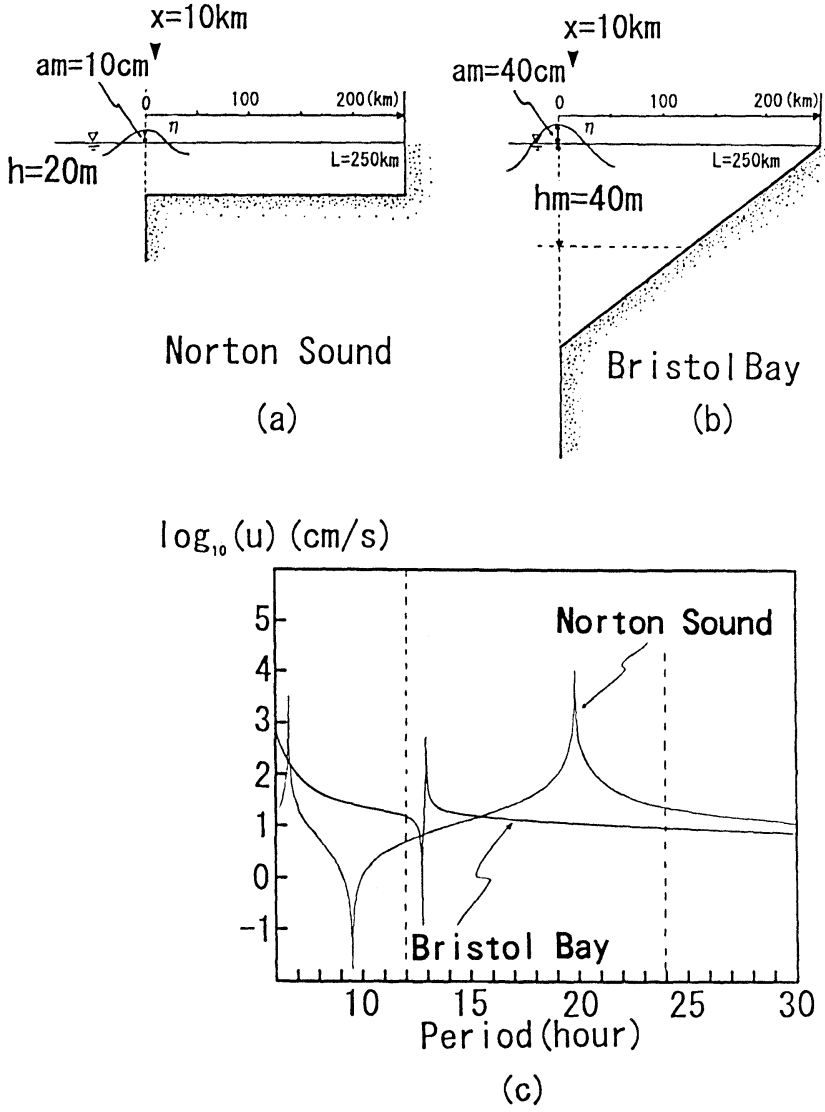

Fig. 9. (a) Depth profile for Norton Sound. (b) Depth profile for Bristol Bay. (c) Theoretical amplitudes of $u(x=10$ km) for each forcing period of Norton Sound and Bristol Bay.

Figure 9 (c) shows the distributions of u ($x=10$ km) for the the forcing period in the simple model of each bay. The peak of the theoretical amplitudes of $u(x=10$ km) is seen at about hour 13 of the forcing period in Bristol Bay. This result indicates that the semidiurnal tidal period is equal to that of the fundamental oscillation in Bristol Bay. Thus, the standing oscillation is generated due to the resonance, and consequently, gives rise to the large amplitudes of u ($x=10$ km). On the other hand, in Norton Sound the peaks of the theoretical amplitudes of u ($x=10$ km) are found at hours 7 and 20 of the forcing period. Since the period of fundamental oscillation is near the diurnal tidal period, the resonance also occurs in the bay over the diurnal forcing period. The resulting theoretical amplitudes are thus larger than those in Bristol Bay, as shown in Fig. 9(c). These calculated amplitudes of tidal current can be brought into close agreement with those of our realistic model quantitatively.

Collectively, these results from the simple one-dimensional model suggest that the difference between the predominant tidal currents for each forcing period in Bristol Bay and the comparable currents in Norton Sound may be attribute not to bottom friction but to the co-oscillations of the tides in each bay.

4.2 The predominant diurnal tidal currents along the shelf slope area

The calculated amplitudes, as shown in Fig. 8(b), of the diurnal tidal current along the shelf slope are substantially larger than those on the shelf, even though there is only a small change in sea level. In addition, since the inertial period of 13.9 hours at the latitude of this study area is shorter than a diurnal-period, no inertial-gravity waves can be considered to propagate along the shelf slope. We believe that this fluctuation in tidal current is driven by a topographic Rossby wave. Thus, it is would also seen that the energy of the tidal current is trapped in the area of the steep shelf slope. Using a theoretical model by BUCHWALD and ADAMS (1968), we next examine the dispersion relation of the topographic Rossby wave trapped on the shelf edge. The topography consists of an exponential shelf slope connecting to the shelf and open ocean of constant depth of 2000 m (Fig. 10(a)). We assume an infinite, straight shelf edge and a depth dependent on offshore distance only. Figure 10(b) shows the theoretical dispersion curves for the 1st mode, and Fig. 10(c) shows this model's phase speed and group velocity. Since the group velocity is much lower than the phase speed at period=24 hours ($\omega/f=0.6$), it follows that the energy of the diurnal tidal current is trapped along the shelf slope. The theoretical wavelength of the diurnal tide has a value of about 400 km as determined from the dispersion curve (Fig. 10(b)), and the phase speed for the period of 24 hours is about 4 m•s^{-1} (Fig. 10(c)). We estimate the relative vorticity ($V_x - U_y$) for the transect A-A'(Fig. 4) along the shelfbreak in order to investigate the temporal and spatial variabilities. The space-time diagram of the relative vorticity is illustrated in Fig. 11. The contour lines for the relative vorticity suggest a northwestward propagation along the shelf

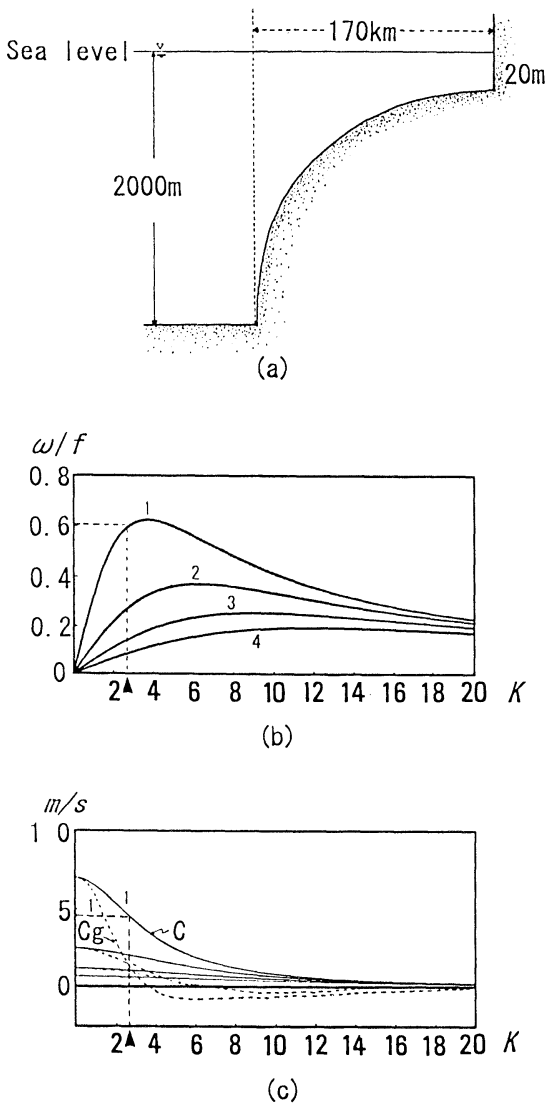

Fig. 10. The x-axis is taken along the bay. (a) The form of the depth profile. (b) Dispersion curves. K is a nondimensional wave number based on width of shelf (L=170 km). The y-axis is a nondimensional frequency based on the Coriolis parameter (f), (c) Phase velocity (C) and group velocity (Cg)

break at a speed of about 4 m•s^{-1} and a wavelength of about 350 km. This theoretical phase speed of the 1st mode topographic Rossby wave model is consistent with that of the diurnal tidal current fluctuations at the shelf slope.

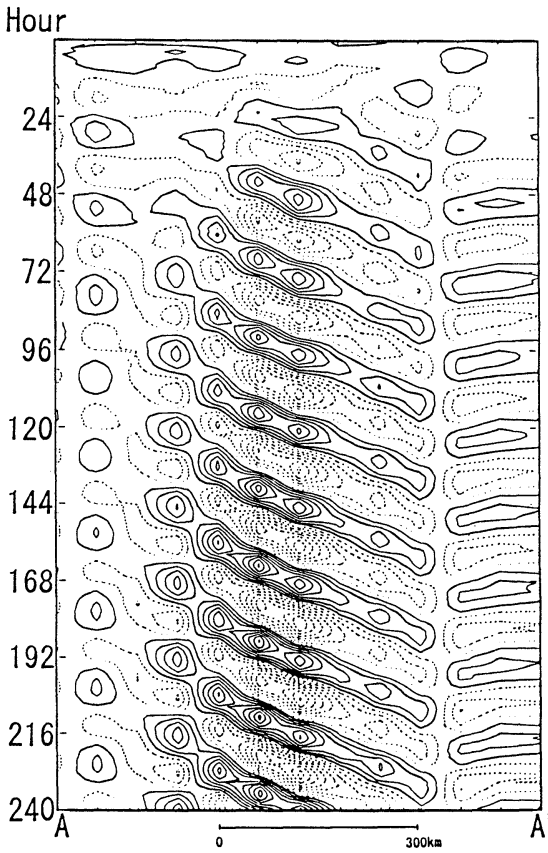

Fig. 11. Space-time diagram along the shelf slope (line *A*–*A'* in Fig. 4) for the vorticity of the period of 24 hour. Positive (negative) vorticities are shown by solid (broken) lines.

These calculated characteristics of the diurnal tidal current on the shelf slope well reproduce those actual characteristics observed by SCHUMACHER and REED (1992). Therefore, this feature suggests one evidence that the predominant diurnal tidal current fluctuations may cause the topographic Rossby wave.

4.3 Spatial distributions of potential energy anomaly and parameter log (H/U³)

The tidal front along the coast of Alaska separates a well-mixed coastal region from a stratified middle region. MUENCH (1976) first suggested that the tidal front exists only near Bristol Bay over the shelf. SCHUMACHER and KINDER (1979) confirmed the existence of such a front along the coast of Alaska, and calculated the parameter log $(H/U^3)=3.5$ at the front near Nunivak Island. As shown in Figs. 3 (a), (b) and (c), the tidal front is also seen in the averaged vertical sections of temperature, salinity, and density.

Here, we calculate the parameter $\log(H/U^3)$ using our model results over the whole shelf for purpose of comparison with the spatial distributions of the potential energy anomaly. This potential energy anomaly for a density stratifica-tion relative to its well-mixed state is defined by the following equations :

$$\bar{\rho} = \frac{g}{H}\int_{-H}^{0}\rho(z)dz \tag{8}$$

$$V = \frac{g}{H}\int_{-H}^{0}(\rho(z)-\bar{\rho})zdz \tag{9}$$

where V is the potential energy anomaly, $\rho(z)$ the density in each layer, $\bar{\rho}$ the averaged density for the water column, g the acceleration of gravity, and H the water depth.

Figure 12 shows the spatial distribution of potential energy anomaly over the eastern Bering Sea shelf based on hydrographic data gathered over a period of 30 years (1963–1992). The potential energy anomaly is less than 1.0 near the coast of Alaska and around the Nunivak Islands. These regions are well-mixed states, as shown in the vertical sections of Fig. 3. The value of the potential energy anomaly gradually increases from the coast of Alaska toward the shelf break. The potential energy anomaly corresponding to the tidal front has a value of 1.0～1.5, which is distributed parallel to about 60 m isobath over the shelf (cf. Fig. 4).

We used the calculated current amplitudes (U) of the semidiurnal and diurnal tides and the depth (H) to estimate the spatial distributions of $\log(H/U^3)$. Since the amplitudes of the N2 and 01 tidal currents are, respectively, 31% of the M_2 tidal current and 61% of the K_1 tidal current (see PEARSON *et al.*, 1981, table 8-1), the sum of the tidal current amplitudes (U) at each grid can be estimated as

$$U=1.31\cdot U_{M2}+1.61\cdot U_{K1} \tag{10}$$

where U_{M2} and U_{K1} are the principal tidal current amplitudes of the M_2 and K_1 tides.

Figure 13 shows the spatial distribution of

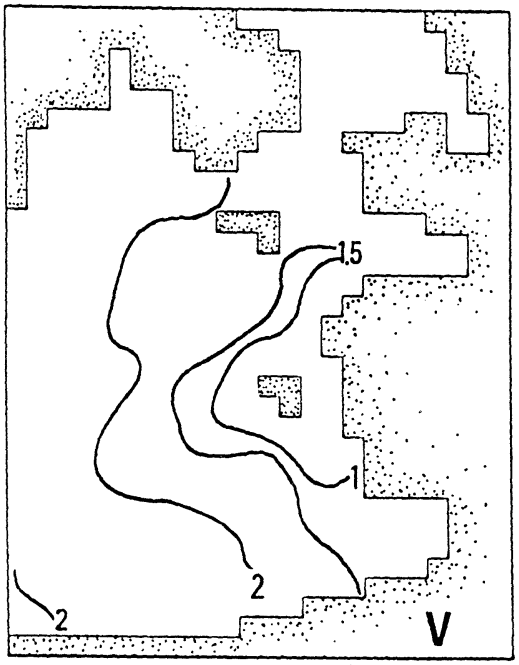

Fig. 12. Spatial distribution of the potential energy anomaly.

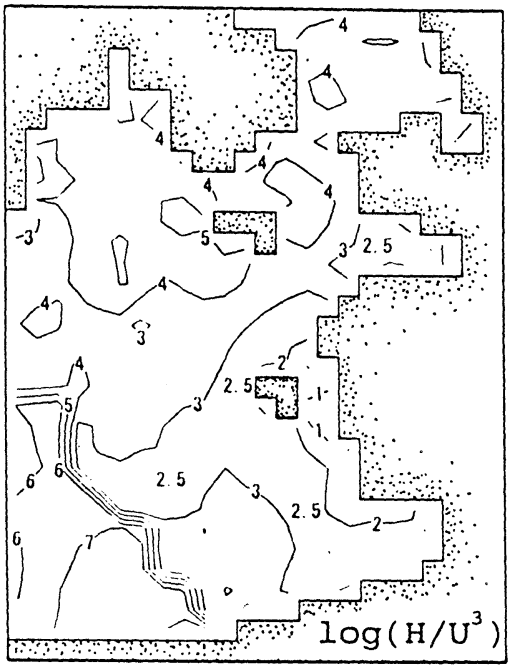

Fig. 13. Spatial distribution of $\log(H/U^3)$ calculated from the model ocean.

$\log(H/U^3)$ over the eastern Bering Sea shelf as derived from the model. A value smaller than $\log(H/U^3)=3.0$ spreads from the south-west area of Nunivak Island to the shelfbreak, and is also found in Bristol Bay and Norton Sound. The value for the Etolin Strait is smaller still, less than $\log(H/U^3)=1.0$, while that around St. Lawrence Island is greater than $\log(H/U^3)=4.0$.

SCHUMACHER and KINDER (1979) showed that a front having the value of $\log(H/U^3)=3.5$ was restricted along the 50 m isobath. However, these authors used the observed value of 25 $cm \cdot s^{-1}$ around the front in their calculation, for our estimation of $\log(H/U^3)$ we used the calculated amplitudes of the semidiurnal and diurnal tidal currents, values which were greater than 35 $cm \cdot s^{-1}$. Consequently, the relatively small value of $\log(H/U^3)=2.5\sim3.0$ appears from the coast of Alaska to the shelf slope. Because the parameter $\log(H/U^3)$ is highly sensitive to the choice of tidal current amplitudes, the difference in amplitude may have caused that between the SCHUMACHER and KINDER's observed and our estimated distribution of $\log(H/U^3)$.

A comparison between the spatial distributions of $\log(H/U^3)$ (Fig. 13) and those of the potential energy anomaly (Fig. 12) reveals the following. The contour lines of $\log(H/U^3)=2.5\sim3.0$ along the coast of Alaska and Bristol Bay, where the tidal front is seen, run parallel to those of the potential energy anomaly. These distributions suggest that the tidal current may control the mixing process in these regions. Although the small potential energy anomaly 1.6 north of St. Lawrence indicates very weak stratification, the tidal mixing energy is relatively small here. This result would suggest that the density structure north of St.Lawrence Island cannot be explained by tidal mixing. As COACHMAN and SHIGAEV (1988) noted, the Bering Slope Current comes into this region, and the Anadyr Current flows through the Bering Strait (KINDER *et al.*, 1986) and generates the turbulent energy north of St. Lawrence Island. Thus, the stratification downstream from the Anadyr Strait may be weak.

2.5 Conclusions

The calculated cotide, corange distributions, and tidal current ellipses for the semidiurnal and diurnal constituents agreed well with the observed ones. The finding obtained in the present study can be summarized as follows :

(1) The semidiurnal tidal current dominates in Bristol Bay, while the diurnal tidal current is predominant in Norton Sound. In both cases, the co-oscillating tide varies according to tidal period. The difference in predominant tidal current between Norton Sound and Bristol Bay can be attributed to the different forcing periods of the respective co-oscillating tides.

(2) Our model shows a relatively large diurnal tidal current rather than a semidiurnal tidal current along the shelf slope, and predicts large tidal current fluctuations propagating northwestward. These results are similar to the observed features for this area. Because the inertial period in this area is shorter than a diurnal-period, the energy of the diurnal tidal current is trapped at the shelf slope. We suggest that these large fluctuations of the diurnal tidal current behave like a 1st mode topographic Rossby wave.

(3) The parameter log (H/U^3) along the coast of Alaska and Bristol Bay gradually increases with offshore, as does the potential energy anomaly. This indicates that stratification near the coast of the Alaskan mainland is dependent on tidal current mixing. On the other hand, the strength of the stratification cannot be explained by the dissipation of tidal energy at the north Bering Sea shelf. Although the parameter $\log(H/U^3)$ is relatively large north of St. Lawrence Island, the water column seems to have weak stratification. In this area, the Anadyr current may break down the density stratification.

Acknowledgements

We would very much like to thank Prof. K. OHTANI, Dr. H. MIYAKE, and Mr. T. MURAKAMI for their useful discussion during this study. We also thank an anonymous referee for helpful comments on drafts of the manuscript.

Reference

BUCHWALD, V. T. and J. K. ADAMES (1968): The propagation of continental shelf wave. Proc. Roy. Soc., **A305**, 235-250.

COACHMAN, L. K. and R. L. CHARNELL (1979): On the lateral water mass interaction-a case study, Bristol Bay, Alaska. J. Phys. Oceanogr., **9**, 278-297.

COACHMAN, L. K. and V. V. SHIGAEV (1988): Northern Bering-Chukchi Sea Ecosystem: The Physical Basis, Results of the third joint US-USSR Bering & Chukchi Seas expedition (BERPAC) summer 1988. United states department of the interior/Fish and Wildlife Service, pp. 17-27.

Faculty of Fisheries, Hokkaido University (1964-1993): Date record of oceanographic observations and exploratory fishing. No. 7-36.

FEARNHEAD, P. G. (1975): On the formation of fronts by tidal mixing around the British Isles. Deep-Sea Res., **22**, 311-322.

JAMES, I. D. (1977): A model of the annual cycle of temperature in a frontal region of the Celtic Sea. Estuarine Coastal Mar. Sci., **5**, 339-353.

KINDER, T.H., D.C. CHAPMAN and J.A. WHITEHEAD (1986): Westward intensification of the mean circulation on the Bering Sea shelf. J. Phys. Oceanogr., **16**, 1217-1229.

LIU, S.-K. and J. J. LEENDERTSE (1982): A three-dimensional shelf model of the Bering and Chukchi sea. 18th conference on Coastal Engineering, America Society of Civil Engineers, New York, pp. 598-616.

LIU, S.-K. and J. J. LEENDERTSE (1986): Modeling the Alaskan coastal waters, *In* Three-Dimensional Shelf Models, N. HEAPS(ed.), (AGU), Washington, D.C.

MOFJELD, H. O. (1986): Observed tides on the northeastern Bering Sea shelf. J. Geophys. Res., **91**, 2593-2606.

MUENCH, R. D. (1976): A note on the eastern Bering Sea Hydrographic structure, August 1974. Deep Sea Res., **23**, 245-247.

OHTANI, K. (1973): Oceanographic structure in the Bering Sea. Memoris. Fac. Fish. Hokkaido Univ. **21**, 65-106.

PEARSON, C. A., H. O. MOFJELD and R. B. TRIPP (1981): Tide of the eastern Bering Sea shelf. p.111-130. *In* The Eastern Bering Sea Shelf: Oceanography and Resources. Vol. 1, HOOD D. W. and J. A. CALDER(eds.), University of Washington Press, Seattle, Wash.

PINGREE, R. D. and D. K. GRIFFITHS (1974): Tidal fronts on the shelf seas around the British isles. J. Geophys. Res., **83**, 4615-4622.

SCHUMACHER. J. D. and T. H. KINDER (1979): A structural over the continental shelf of eastern Bering Sea, J. Phys. Oceanogr., **9**, 79-87.

SCHUMACHER, J. D. and T. H. KINDER (1983): Low-frequency flow regimes over the Bering Sea Shelf, J.

Phys. Oceanogr., **13**, 607–623.

SCHUMACHER, J. D. and R. K. Reed (1992): Characteristics of current over the continental slope of Bering Sea, J. Geophys. Res., **97**, 9423–9433.

SIMPSON, J. H. (1971): Density stratification and microstructure in the western Irish Sea. Deep–Sea Res., **18**, 309–319.

SIMPSON, J. H. and J. R. Hanter (1974): Fronts in the Irish Sea. Nature, **250**, 404–406.

SIMPSON, J. H., C. M. ALLEN and N. C. G. MORRIS (1978): Fronts on the continental Shelf. J. Geophys. Res., **83**, 4607–4614.

SÜNDERMANN, J. (1977): The semidiurnal lunar tide M_2 in the Bering Sea. Dtsch. Hydrogr. Z., **30**, 91–101.

UNOKI, S. and I. ISOZAKI (1965): Mean sea level in bays, with special reference to the mean slope of sea surface due to the standing oscillation of tide. The Oceanogr. Mag., **17**, 11–35.

Received November 5, 1996
Accepted May 8, 1997